

Magnetic properties of poly(trimethylene terephthalate-*block*-poly(tetramethylene oxide) copolymer nanocomposites reinforced by graphene oxide-Fe₃O₄ hybrid nanoparticles

Anna Szymczyk^a, Sandra Paszkiewicz^b, Janusz Typek^a, Zdenko Špitalský^c, Izabela Janowska^d,
Grzegorz Żołnierkiewicz^a, Nikos Guskos^a

^a West Pomeranian University of Technology, Institute of Physics, Piastów Av. 48, PL-70310 Szczecin, Poland

^b West Pomeranian University of Technology, Institute of Material Science and Engineering, Piastów Av. 19, PL-70310 Szczecin, Poland

^c Polymer Institute, Slovak Academy of Sciences, Dúbravská cesta 9, 845 41 Bratislava 45, Slovakia

^d Institute of Chemistry and Processes for Energy, Environment and Health (ICPEES), CNRS and University of Strasbourg, 25 rue Becquerel, 67087 Strasbourg Cedex 2, France

*Corresponding author. Tel.: +48 91 449 45 81; e-mail address: aszymczyk@zut.edu.pl

Abstract: Thermoplastic elastomeric nanocomposites based on poly(trimethylene terephthalate-*block*-poly(tetramethylene oxide) copolymer (PTT-PTMO) and graphene oxide-Fe₃O₄ nanoparticle hybrid were prepared by *in situ* polymerization. Superparamagnetic GO-Fe₃O₄ hybrid nanoparticles before introducing to elastomeric matrix were characterized by X-ray photoelectron spectroscopy (XPS), X-ray diffraction (XRD), thermogravimetric analysis (TGA) and scanning electron microscopy (SEM). The effect of loading (0.3 and 0.5 wt %) of GO-Fe₃O₄ nanoparticle hybrid on the phase structure, tensile and magnetic properties of synthesized nanocomposites was investigated. The phase structure of nanocomposites was evaluated by differential scanning calorimetry (DSC) and dynamic mechanical thermal analysis (DMTA). Dispersion of GO-Fe₃O₄ nanoparticles in elastomeric matrix was evaluated by transmission electron microscopy (TEM). Magnetic properties of GO-Fe₃O₄ nanoparticle hybrid and nanocomposites with their content were characterized by using two different

techniques: dc SQUID magnetization measurements as a function of temperature (from 2 to 300 K) and external magnetic field and ferromagnetic resonance (FMR) at microwave frequency.

Keywords: polymer nanocomposites, graphene oxide-Fe₃O₄ nanoparticle hybrid, polyester thermoplastic elastomer, phase structure, magnetic properties.

1. Introduction

The interest in magnetic nanoparticles based on iron oxides is enormous due to their wide range of potential applications, especially in biomedicine, catalysis, waste water treatment, energy storage, and spintronics [1-9]. Magnetite (Fe₃O₄) and maghemite (γ -Fe₂O₃) are the most important ferromagnetic compounds among all iron oxides [10]. Saturation magnetization of magnetite reaches 92 emu g⁻¹ at room temperature (RT) in bulk material. On the other hand, maghemite is more stable than magnetite, more biocompatible, although presenting bulk saturation magnetization slightly smaller. The chemical formulae for stoichiometric magnetite can be written as (8Fe³⁺)_{tetra}[8Fe²⁺+8Fe³⁺]_{octa}32O²⁻, where the subscripts tetra and octa mean tetrahedral (A sites) and octahedral (B sites) interstitials, respectively. Below 851 K magnetite is ferrimagnetic with A-site magnetic moments aligned antiparallel to the B-sites. At 120 K magnetite undergoes a first-order phase transition (Verwey transition), with a change of crystal structure, latent heat and decrease of the dc conductivity. The distribution of Fe³⁺ and Fe²⁺ in B sites changes from a dynamic disorder to a long-range order with an orthorhombic symmetry below 120 K. To study the magnetic properties of magnetite nanoparticles different experimental techniques were used. The basic and most often applied is the static (dc) and dynamic (ac) magnetometry employing vibrating sample and SQUID method. Two resonance techniques - ferromagnetic resonance (FMR) and Mössbauer spectroscopy usually deliver complementary magnetic characteristics [11-29].

Recent intense research on graphene and its derivatives follows the trend of exploration of novel low dimensional systems and is driven by possible promising applications of graphene-based magnets in spintronics. However, due to delocalized π bonding network graphene lacks localized magnetic moments and is intrinsically non-magnetic. Magnetic resonance spectroscopy measurements have

confirmed theoretical predictions that in a single-layer graphene the carrier mediated exchange interaction leads to antiferromagnetic coupling [30]. The same experimental technique was used to study the magnetic correlations at zig-zag edges of a single-layer graphene [31]. It was found that the zig-zag spins are ferromagnetically correlated. Point defects such as the zig-zag edge states, vacancies with the trapped electron or chemical doping of foreign atoms, can introduce magnetic moments, but make the structure stability of graphene lower. Despite the efforts of increasing the magnetism of graphene materials, they usually display a weak Curie-type paramagnetism and magnetization below 0.2 emu/g. Recently, it has been demonstrated that N-doping of graphene oxide (GO) can dramatically increase its magnetization up to 1.66 emu/g and makes the magnetism of GO change from purely spin-half paramagnetism to ferromagnetism with Curie temperature of ca. 100 K [8]. In another work it has been shown that it is also possible to inject spins to a single layer graphene from an adjacent ferromagnetic material (dynamical spin injection) [32]. A pure spin current was pumped into graphene from the processing magnetization of the ferromagnet with very high efficiency.

Many researchers have shown that integrating GO or reduced graphene oxide (RGO) with inorganic nanoparticles allows for the properties of the nanocomposite to be engineered for specific applications. For example, a new type of hybrid material – graphene/Fe₃O₄ – has been recently synthesized and found a broad range of applications e.g. in targeted drug delivery, magnetic resonance imaging, lithium-ion batteries, ion removal, sensor, catalysts, etc. [32, 33]. These multifunctional nanomaterials combine the beneficial effects of graphene - high conductivity and large surface-to-volume ratio - with strong magnetism, low price and low environmental toxicity of magnetite. Magnetic properties of GO-Fe₃O₄ nanocomposites have been investigated by measuring magnetization of produced samples in an external magnetic field [34-37]. At room temperature (RT) no magnetic hysteresis loop was observed, as expected, because the nanocomposite's blocking temperature was below RT. Saturation magnetization smaller than in magnetite nanoparticles was explained by low loading of Fe₃O₄ in nanocomposite. In each studied nanocomposite monodispersed magnetite nanoparticles were successfully attached to graphene sheets [37].

Graphene magnetic nanocomposites include also more complex systems such as Cu/RGO/Fe₃O₄ [38, 39, 40], Ag/RGO/Fe₃O₄ [41], Pd/RGO/Fe₃O₄ [42, 43] hybrids which were recently synthesized using plant extracts as biological materials under mild conditions. These hybrid nanocomposites can be used as magnetically separable and reusable catalyst for cyanation of aldehydes to nitriles [38] or for the reduction of 4-nitrophenol and organic dyes [39-43].

The dispersion of the highly exfoliated GO nanoplates decorated by Fe₃O₄ nanocrystals in polymer matrix is the crucial factor that determine the quality and reliability of nanocomposites and their expected magnetic properties. Shen et al. [44] have shown lightweight, multifunctional polyetherimide/graphene-Fe₃O₄ composites foams for shielding of electromagnetic pollution.

Our recent studies have shown that introduction of small amount (up to 0.5 wt. %) of highly exfoliated GO [45], graphene nanoplatelets (GNP) or hybrid system being a mixture of GNP and single-walled carbon nanotubes (SWCNT) [46-48] into polyester elastomeric nanocomposites improved their mechanical properties and can provide them new functional properties as electrical and thermal conductivity.

In this work, a superparamagnetic GO-Fe₃O₄ hybrid nanoparticles were prepared and used as nanofiller for polyester thermoplastic elastomeric matrix. The magnetic properties of the polyester thermoplastic polymer nanocomposite reinforced by GO-Fe₃O₄ nanoparticles hybrid were characterized by using two different techniques: dc SQUID magnetization measurements as a function of temperature and external magnetic field, and ferromagnetic resonance (FMR) at microwave frequency. The results of measurements are correlated with morphological features of the studied samples.

2. Experimental

2.1 Materials

Ferric chloride hexahydrate (FeCl₃·6H₂O), ferrous chloride tetrahydrate (FeCl₂·4H₂O), ammonium hydroxide, dimethyl terephthalate (DMT), poly(tetramethylene oxide) glycol (PTMG) with molecular weight of 1000 g mol⁻¹, tetrabutyl orthotitanate (TBT) were delivered by Sigma-

Aldrich and used as received. Bio-1,3-propanediol (bio-PDO, Susterra®Propanediol) was purchased from DuPont Tate&Lyle (USA). Antioxidant Irganox 1010 was purchased from Ciba-Geigy (Switzerland). The GO nanoplatelets used for preparation of nanoparticle hybrid were prepared by a modified Hummers method [49]. For GO synthesis the expanded graphite with an average size of 5 μm from (SGL Carbon, Germany) was used.

2.2 Preparation of GO-Fe₃O₄ hybrid structures and their characterization

The GO-Fe₃O₄ hybrid nanoparticles were synthesized by inverse chemical co-precipitation method according to the following procedure [50]. 50 mg of GO powder was exfoliated in 150 mL of deionized water by ultrasonic treatment for 30 min. and followed by the addition of 1.6 g FeCl₃·6H₂O and 0.6 g FeCl₂·4H₂O. The mixture solution was added dropwise into 250 mL three-necked flask containing 25 mL of 30 % ammonium hydroxide under vigorous mechanical stirring. To prevent oxidative reaction, the system was kept under nitrogen atmosphere. The resulting black solution was maintained at 80 °C for 1 h and then cooled to RT. The black precipitate was isolated by a permanent magnet and washed three times with deionized water and three times with ethanol. The collected magnetic material was dried at 50 °C in vacuum.

2.3 Synthesis of PTT-PTMO/GO-Fe₃O₄ nanocomposites

PTT-PTMO/GO-Fe₃O₄ nanocomposites were synthesized by a two-step polycondensation reaction of dimethyl terephthalate (DMT, Sigma-Aldrich), bio-1,3-propanediol (bio-PDO) and poly(tetramethylene oxide) glycol (PTMG) in the presence of TBT as catalyst and Irganox 1010 as an antioxidant. Details of the preparation method of PTT-PTMO based nanocomposites could be found in our previous publications concerning GO [45] and a hybrid system of GNP and SWCNT [47]. Before carrying the polymerization, a dispersion of GO-Fe₃O₄ has been prepared by dispersing the appropriate amount of functionalized graphene nanoplatelets in bio-PDO through ultrasonication for 15 min using laboratory homogenizer (Sonoplus HD 2200, with frequency of 20 kHz and 75% of power 200W) and subsequent intensive mixing for 15 min using high-speed stirrer (Ultra-Turax T25).

The content of rigid PTT and soft PTMO segments was approximately the same (i.e. 50 wt % of each).

2.3 Characterization

The synthesized GO-Fe₃O₄ has been characterized by X-ray photoelectron spectroscopy (XPS) performed on Kratos Axis ULTRA X-Ray photoelectron spectrometer equipped with monochromatic Al K α (h ν =1486.6 eV) radiation to quantitatively analyze the chemical composition of the nanofiller.

X-ray diffraction (XRD) data were obtained using the X'Pert PAN analytical diffractometer employing Cu K α radiation (λ =0.15406 nm) at an operating voltage and current of 40 kV and 40 mA, respectively. The nanocrystal size (d) was estimated according to Sherrer's equation [51]

$$d = K\lambda/B\cos\theta \quad (1)$$

where K is the Scherrer constant (0.89), B is the full width at half maximum (FWHM) of the strongest reflection peak, and θ is the diffraction angle.

Thermogravimetric analysis (TGA) was performed using a SETARAM TGA 92-16 instrument in air flow (20 mL min⁻¹) using a heating rate of 10 K min⁻¹ in a temperature range from 298 K up to 1073 K. Indium and aluminum were used for temperature calibration. The amount of applied samples was ~ 10 mg. Two paralleled runs were performed for each sample. The surface morphology of the GO and GO-Fe₃O₄ was observed by Dual Beam (FIB/SEM) Microscope Quanta 3D 200i (FEI).

The microstructure of nanocomposites was observed by transmission electron microscopy (TEM) on Topcon 002B - UHR microscope working with an accelerated voltage of 200 kV and a point-to-point resolution of 0.17 nm. Prior to the analysis thin slices of polymers were prepared by cryo-cutting technique and deposited on the copper grid.

The thermal transitions of neat copolymer and prepared nanocomposites were investigated with differential scanning calorimetry (DSC) on a Q100 thermal analyzer (TA Instruments). A standard heat-cool-heat program with heating/cooling rate of 10 K min⁻¹ was performed between 173

and 523 K. The cooling and second heating scans were used in order to determine the glass transition temperature, crystallization and melting peaks. The degree of crystallinity (x_c) has been calculated using the following equation:

$$x_c = 100 \times (\Delta H_m / \Delta H_m^o) \quad (2)$$

where ΔH_m is the melting peak area of an examined sample on DSC thermograms, and ΔH_m^o is the enthalpy of fusion (146 J/g [52]) of fully 100 % crystalline PTT.

The dynamic mechanical thermal analysis (DMTA) has been performed using a Polymer Laboratories MK II apparatus working in a bending mode. The samples were heated in the temperature range from 153 K to the polymer melting temperature and the heating rate of 3 K min⁻¹ at a frequency of 1 Hz was used.

The tensile and cyclic tensile properties of nanocomposites were performed on an Autograph AG-X plus (Shimadzu) tensile testing machine equipped with a 1 kN Shimadzu load cell, an contact optical long travel extensometer and the TRAPEZIUM X computer software, operated at a constant crosshead speed of 100 mm min⁻¹. Measurements on dumbbell samples were performed at RT with the grip distance of 20 mm according to DIN 53455 standard. The values of yield strength, stress and elongation at break, permanent set (with error bars representing the 95 % confidence interval) were calculated from the stress–strain curves.

MPMS-7 SQUID magnetometer was used for dc magnetization measurements in the 2 - 300 K temperature range in the zero-field-cooled (ZFC) and field-cooled (FC) modes and for isothermal ($T = 2, 300$ K) magnetization in magnetic fields up to 70 kOe. Magnetic resonance study was carried out on a conventional X–band ($\nu = 9.4$ GHz) Bruker E 500 spectrometer with the 100 kHz magnetic field modulation. The ferromagnetic resonance (FMR) spectra were taken in the 90 – 290 K range and were in the form of the first derivatives of microwave absorption with respect to the sweeping external magnetic field.

3. Results and discussion

3.1 Structural characterization of GO-Fe₃O₄ nanoparticle hybrid

XPS has been employed to analyze the nature and the relative amount of iron and oxygen-containing functional groups present on the graphene surface. C1s XPS spectrum of GO synthesized via Hummers method is as follows: sp²-C: 6.09 %; sp³-C: 42.26 %; C-O: 18.49 %; C=O: 24.32 %; O-C=O: 4.40 %; π-π: 1.16 %. For GO-Fe₃O₄, C1s XPS spectrum shows: sp²-C: 56.59 %; sp³-C: 23.91 %; C-O: 9.65 %; C=O: 4.57 %; O-C=O: 4.15 %; π-π: 1.13 %. Whereas, the O1s XPS spectrum (**Figure S1**) shows: FeO_x: 66.88 %, C=O/Fe-OH: 16.27 %; C-O: 13.27 %. After successful functionalization of Fe₃O₄, clearly visible changes in C1s XPS spectrum were observed. An increase of sp² hybridized carbons from 6.09 to 56.59 %, and at the very same time a decrease in sp³ hybridized carbons from 42.26 to 23.91 %, can be noted. The XPS spectrum of GO-Fe₃O₄ consists of functional groups such as sp² (C=C), epoxy/hydroxyl (C-O), carbonyl (C=O) and carboxylates (O-C=O) [53]. Moreover, in the case of GO-Fe₃O₄, XPS spectra indicate the presence of FeO_x in the amount of 66.88 %, which certainly points to the chemical incorporation of iron oxide.

In order to confirm the attachment of Fe₃O₄ nanocrystals on the surface of GO the thermogravimetric analysis in air was performed on as-received GO, GO-Fe₃O₄ hybrid and Fe₃O₄ nanoparticles. The Fe₃O₄ nanocrystals content in the GO-Fe₃O₄ hybrid can be estimated from the residual weight percentages. The total weight loss of the Fe₃O₄ nanoparticles is 3.3 % (**Figure 1a**) for the whole temperature range because of the removal of adsorbed physical and chemical water. As can be seen in Fig. 1a, the TGA curves of GO show a three-step weight loss between 273 to 1073 K with a total weight loss of ~98 %, while GO-Fe₃O₄ hybrid in this temperature range undergoes a weight loss of 29.6 %, which is closely related to the oxidation of GO and confirms high concentration of Fe₃O₄ nanocrystals (~70 wt %) on GO nanosheets.

Figure 1b shows X-ray diffractograms of GO-Fe₃O₄ and Fe₃O₄ nanoparticles synthesized in the same conditions. The diffraction peaks at 30.26, 35.60, 43.35, 53.76, 57.25, 62.95 ° correspond to the (220), (311), (400), (422), (511), (440) and are in good accordance with the inverse cubic spinel phase of Fe₃O₄ (magnetite, JCPDS card no. 85-1436) [51]. Using the most intense reflection (311), the average size of Fe₃O₄ nanocrystals at GO surface was calculated to be ca. 8.9 nm. In our earlier

work it was shown that the GO powder has characteristic diffraction peak at $2\theta \sim 10^\circ$ attributed to the (001) reflexion [54]. The disappearance of this peak in XRD pattern of GO-Fe₃O₄ hybrid suggests that the layer stacking of the GO sheets has been destroyed by the loading of Fe₃O₄ nanocrystals.

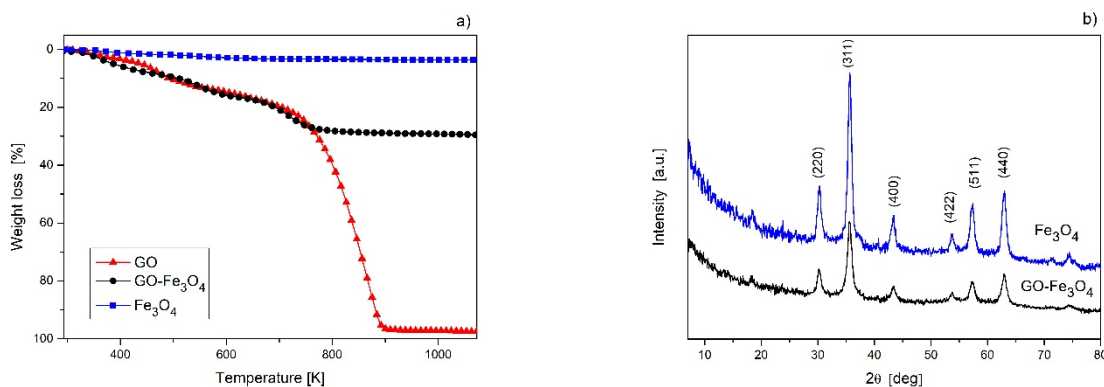


Figure 1. a) TGA curves of GO, GO-Fe₃O₄ nanoparticle hybrid and nano-Fe₃O₄; and b) X-ray diffraction pattern of GO-Fe₃O₄ and Fe₃O₄ synthesized in the same conditions.

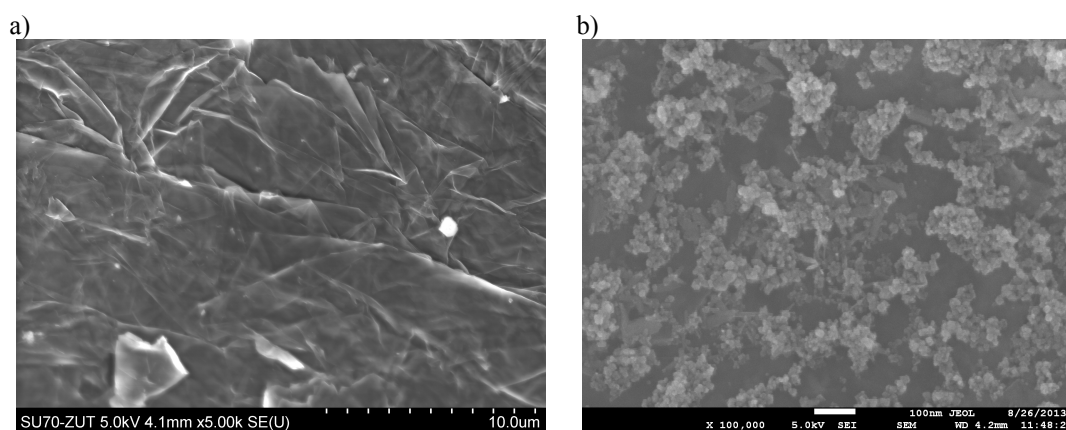


Figure 2. SEM images of as received GO (a) and GO-Fe₃O₄ (b).

The morphology of synthesized GO-Fe₃O₄ nanoparticle hybrid and GO used for their preparation was characterized by SEM. As shown in **Figure 2a**, the surface morphology of GO resembles strongly folded curtain, what indicates that GO flakes were rather overlapped than aggregated. On the other hand, when the synthesis of GO-Fe₃O₄ was carried out by an inverse chemical co-precipitation method, the formation of Fe₃O₄ took place on the graphene oxide sheets. SEM image (**Figure 2b**) shows that these Fe₃O₄ nanoparticles are densely distributed on GO sheets and they are not separated but decorated in bunches on the curled and thin wrinkled sheets, having a rather uniform distribution

on the surface of GO. It can be observed from the SEM images that the average diameter of Fe₃O₄ nanocrystals at GO surface was around 10 nm, which is close to the value determined from XRD pattern.

3.2 Dispersion of GO-Fe₃O₄ in the PTT-PTMO matrix

The distribution of GO-Fe₃O₄ in PTT-PTMO copolymer matrix was studied by TEM microscopy. Representative images of nanocomposites containing 0.5 wt % of GO-Fe₃O₄ are presented in **Figure 3**. Nanocomposites exhibit rather uniform distribution of GO-Fe₃O₄ in the matrix (**Figures 3a-e**) and there were no large areas of graphene oxide that were not decorated with Fe₃O₄ nanoparticles. The high transparency of the GO sheets indicate that GO was well exfoliated into few layered sheets decorated by Fe₃O₄ nanocrystals. The observed morphology of GO-Fe₃O₄ at higher magnification have shown the sphere-like nanoparticles with sizes from 4 to 16 nm (**Figures 3b-c, e**) distributed on the surface of the GO sheets. Based on a total number of (N=124) particle sizes determined from several TEM images (**Figure 3f**) an average Fe₃O₄ particle size of 9 nm (2.1 nm) was estimated, which is in good agreement with the particles size determined from XRD data. Locally the areas with a more densely distributed nanoparticles (**Figure 3d**) were also observed. Likewise, the edges of GO flakes of several sheets can be clearly observed in **Figure 3c**. It can also be noted that Fe₃O₄ (**Figure 3**) were firmly attached to the graphene oxide sheets, that even a specimen's preparation for TEM analysis didn't affect the samples, which indicates that an excellent adhesion between GO and Fe₃O₄ particles has been achieved. Moreover, the presence of much smaller GO sheets densely decorated by Fe₃O₄ nanocrystals (**Figure 3d**) compared to the size of GO sheets used for preparation of these hybrid, was observed. Probably, due to high concentration of Fe₃O₄ nanocrystals (confirmed by TGA analysis) on GO sheets after inverse co-precipitation, some of them were cut into smaller pieces.

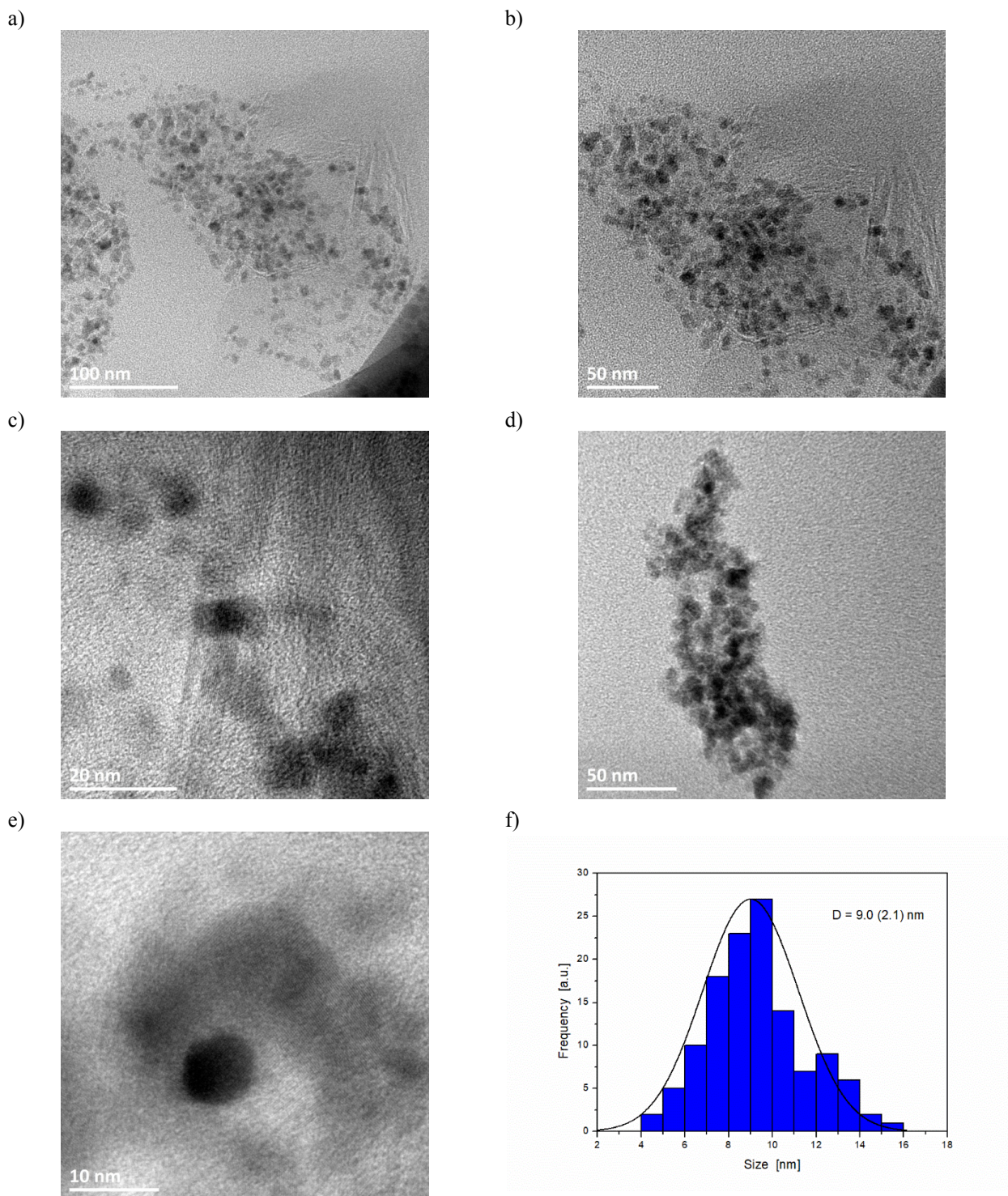


Figure 3. TEM images of the PTT-PTMO nanocomposites with 0.5 wt % of GO-Fe₃O₄ (a-e) and the histogram of distribution of the Fe₃O₄ particle sizes (f).

3.3 Effect of the presence of GO-Fe₃O₄ on phase structure and tensile properties of nanocomposites

In polyester block copolymers the heterophase structure, which can be reproducible in heating-cooling cycles, is responsible for their elastic and thermoplastic properties. The presence of GO-

Fe₃O₄ can affect their micro- and nanophase separation. When a synergy between the crystalline lamellae of polymer and the hybrid nanofiller is created, the improvement of the macroscopic properties of these composites can be expected. Values of intrinsic viscosity $[\eta]$, M_n and polydispersity (**Table 1**) of obtained composites are comparable to the values for the neat block copolymer. These results can indicate that at low loading of nanofillers *in situ* polymerization allows obtaining materials with comparable values of molecular weight, which have no effect on phase separation structure.

Table 1. Characteristics of the synthesized PTT-PTMO based nanocomposites

Sample	GO-Fe ₃ O ₄ [wt %]	$[\eta]$ [dl g ⁻¹]	M_n [g mol ⁻¹]	M_w [g mol ⁻¹]	M_w/M_n
PTT-PTMO	0	1.422	41 720	83 850	2.01
PTT-PTMO/0.3GO-Fe ₃ O ₄	0.3	1.423	42 440	87 850	2.07
PTT-PTMO/0.5GO-Fe ₃ O ₄	0.5	1.420	41 980	88 570	2.11

$[\eta]$ - intrinsic viscosity, M_n - number average molecular weight of the samples after filtration of nanofiller determined by SEC according procedure [44], M_w/M_n – polydispersity

The effect of the presence of GO-Fe₃O₄ in PTT-PTMO matrix on the phase transitions (glass transitions, physical crosslink melting) in the obtained nanocomposites was studied by DMTA and DSC analysis. The storage modulus (E'), loss modulus (E'') and loss factor ($\tan \delta$) as a function of temperature are presented in **Figure 4** for the neat block copolymer and its nanocomposites with GO-Fe₃O₄. Nanocomposites with GO-Fe₃O₄ show similar E' and E'' profiles like the neat block copolymer matrices. Taking into consideration the experiment precision it can be inferred that the rubber moduli for nanocomposites are practically the same as for the neat block copolymer. The $\tan \delta$ curves for all samples show two β - relaxations peaks, β_1 and β_2 . These two relaxations are attributed to the glass transition of polyether-rich (β_1) phase and amorphous polyester (β_2) phase, respectively. It can be seen (**Figure 4, Table 2**), that the β_1 - relaxation in nanocomposites is shifted to lower temperatures in comparison to the neat block copolymer. This confirms that addition of GO-Fe₃O₄ to the copolymer

matrix improves the phase separation in the system. The final sample softening to a polymer melt, during which physical crosslinks (crystalline PTT domains) disrupt, takes place in the range of 450-475 K in all samples.

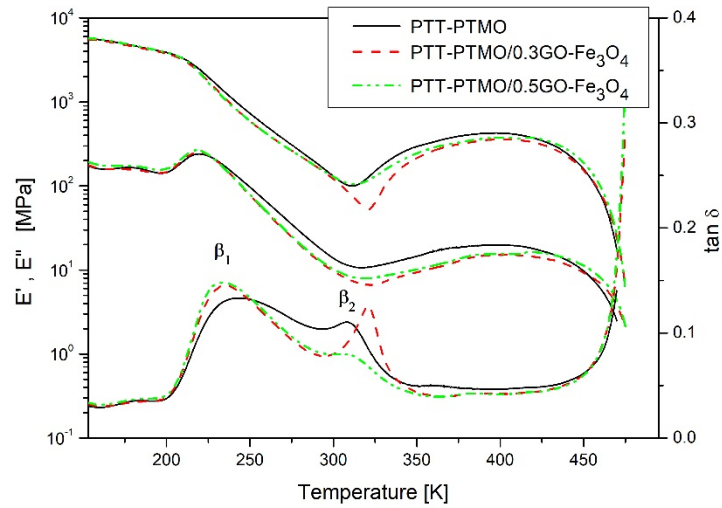


Figure 4. Storage and loss modulus and $\tan \delta$ for neat PTT-PTMO copolymer and PTT-PTMO/GO- Fe_3O_4 nanocomposites containing of 0.3 and 0.5 wt % of GO- Fe_3O_4 .

Table 2. DMTA and DSC data for the obtained nanocomposites

Sample	$T_{\beta 1}$ [K]	$T_{\beta 2}$ [K]	T_{g1} [K]	T_m [K]	ΔH_m [J g ⁻¹]	T_c [K]	ΔH_c [J g ⁻¹]	ΔT [K]	x_c [%]
PTT-PTMO	244	308	207	477	31.9	399	32.1	78	21.8
PTT-PTMO/0.3GO- Fe_3O_4	235	321	205	477	31.1	402	31.4	75	21.3
PTT-PTMO/0.5GO- Fe_3O_4	234	309	205	478	31.6	418	31.6	60	21.6

$T_{\beta 1}, T_{\beta 2}$ – temperatures of β_1 and β_2 -relaxation corresponding to the glass transition temperatures determined from maximum of $\tan \delta$; T_{g1} – glass transition temperature of amorphous soft phase; $T_m, \Delta H_m$ – temperature and enthalpy of melting of polyester phase; x_c – degree of crystallinity; $T_c, \Delta H_c$ – temperature and enthalpy of crystallization of polyester phase, ΔT – degree of supercooling.

In **Figure 5** and **Table 2** the DSC results obtained during cooling and heating of the nanocomposites are presented. DSC data confirm conclusions obtained by DMTA. Herein, the addition of GO- Fe_3O_4 slightly shifted the value of T_{g1} ($T_{\beta 1}$ on DMTA plots) toward lower temperatures. Moreover, no notable effect on the melting temperature (T_m) can be observed. In

contrast, analysis of the cooling scans of nanocomposites and the neat block copolymer indicate that GO-Fe₃O₄ in PTT-PTMO copolymer could improve the crystallization of polymer matrix, since the crystallization temperature increased by 3-19 K. The degree of super cooling ($\Delta T = T_m - T_c$) of nanocomposites is smaller than that of neat PTT-TMO copolymer, which indicate that the presence of GO-Fe₃O₄ in PTT-PTMO block copolymer increases the rate of crystallization of PTT segments in these copolymers. This might be relevant to the processing properties of these materials. On the other hand, however, while the presence of nanoparticles accelerates the formation of crystalline phase, it does not correspond to the melting enthalpy, ΔH_m , and designated on its basis the degree of crystallinity (values of x_c are comparable to one another). It proves that GO-Fe₃O₄, randomly distributed in the copolymer matrix, promotes nucleation of PTT crystallites.

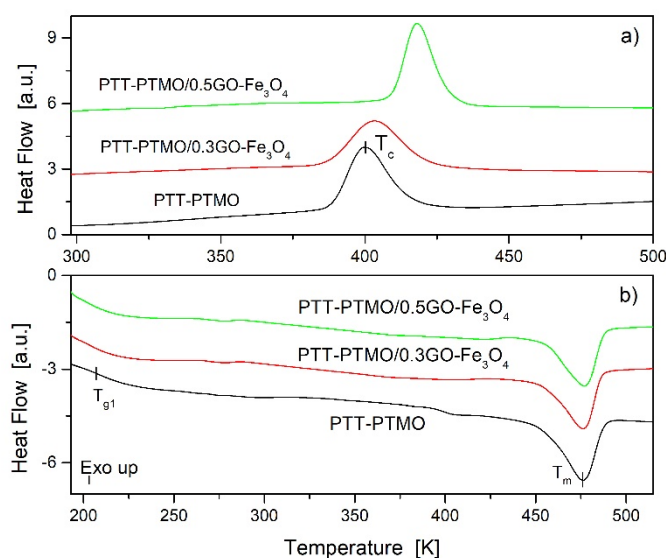


Figure 5. DSC thermograms obtained during cooling (a) and 2nd heating (b) for PTT-PTMO/GO-Fe₃O₄ nanocomposites.

As a result of the presence of GO-Fe₃O₄ and enhancement of phase separation in PTT-PTMO matrix at their low loading, the improvement of tensile and cyclic tensile properties of nanocomposites was observed. The representative stress-strain curves for nanocomposites obtained in the cyclic and non-cyclic uniaxial tensile tests are presented in **Figure 6** and the results are summarized in **Table 3**. The yield stress and tensile strength as well as yield strain and stress at break

of nanocomposites slightly increases with the GO-Fe₃O₄ loading in the copolymer matrix. The values of permanent set (PS) in tension direction resultant from the attained strain of 100 and 200 % (**Table 3, Figure 6b**) for nanocomposites are close (within errors range) to the values obtained of the neat block copolymer.

Table 3. Tensile properties of the PTT-PTMO/GO-Fe₃O₄ nanocomposites

Sample	σ_y (MPa)	ϵ_y (%)	σ_b (MPa)	ϵ_b (%)	PS(100) (%)	PS(200) (%)
PTT-PTMO	12.1 ±0.1	41.7 ±0.1	23.5 ±0.2	622 ±12	38 ±2	95 ±3
PTT-PTMO/0.3GO-Fe ₃ O ₄	12.4 ±0.1	42.7 ±0.1	24.8 ±0.6	668 ±24	38 ±1	93 ±2
PTT-PTMO/0.5GO-Fe ₃ O ₄	12.6 ±0.2	43.2 ±0.3	26.8 ±0.9	680 ±31	38 ±2	95 ±3

σ_y , ϵ_y – yield stress and strain respectively; σ_b - stress at break; ϵ_b -strain at break. PS(100), PS(200) – permanent set was taken as the strain at which zero load was measured on the first unloading cycle to 100% and 200% strain, respectively.

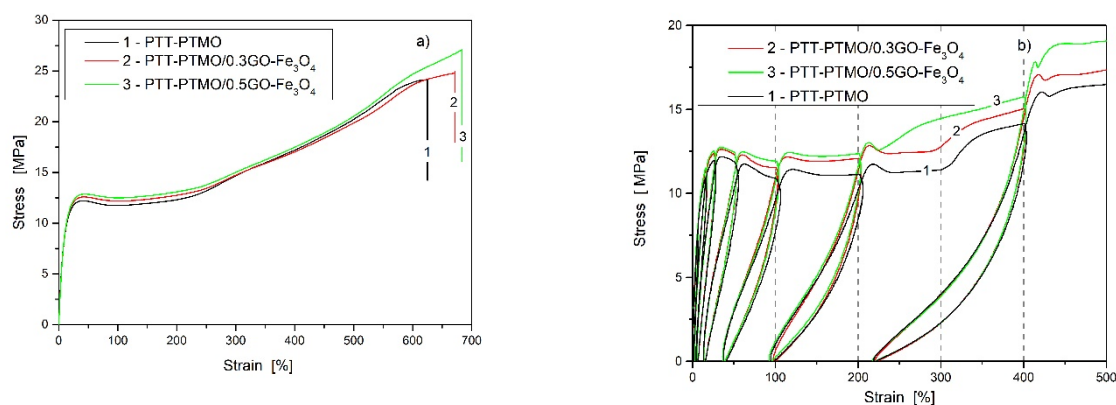


Figure 6. Stress-strain curves for PTT-PTMO/GO-Fe₃O₄ nanocomposites.

3.4 Magnetic properties of GO-Fe₃O₄ nanocomposites

The magnetic properties of PTT-PTMO/GO-Fe₃O₄ nanocomposites and GO-Fe₃O₄ nanoparticles used for their preparation were studied using a SQUID magnetometer in order to investigate the temperature dependence of dc magnetic susceptibility and isothermal magnetization as a function of magnetic field as well as a magnetic resonance spectrometer to examine the ferromagnetic/paramagnetic spectra at microwave frequency.

When sample is cooled to the lowest temperature without external magnetic field (ZFC mode), the magnetic moments of each nanoparticle align along the easy axis in the lattice, and since the crystallites are oriented randomly, the overall magnetic moment of sample will be zero. As the temperature is increased, thermal energy releases some magnetic moments from the easy axis and they will be align along the external field. The magnetocrystalline energy $K \cdot V$ (where K is magnetocrystalline anisotropy energy density constant and V the volume of a nanoparticle) plays a dominate role in that temperature range. At a specific temperature (T_B - blocking temperature) the largest number of moments is aligned along the external field and gives maximum magnetization. Often a simple relation between magnetocrystalline and thermal energy is used to estimate T_B [55]:

$$K \cdot V = 25 k T_B \quad (3)$$

where k is Boltzmann's constant. Above T_B the Zeeman energy $\mu \cdot H$ (where μ is the magnetic moment and H external magnetic field) is smaller than the thermal energy what causes randomization of the moments and the net magnetization will decrease with the increase in temperature (superparamagnetic phase). On the other hand, when sample is cooled from high temperature in the presence small external field (FC mode) the decrease in thermal energy causes orientation of moments along the direction of the field and subsequent increase in magnetization. The ZFC and FC curves coincide or show the same tendency as the temperature is decreased. The situation changes on further cooling below T_B : the Zeeman energy overcomes the thermal energy and causes the moments to orient partially along the applied field, what results in separation of ZFC and FC magnetization curves. At the lowest temperature the Zeeman energy causes the maximum orientation of moments in the field direction and the biggest magnetization.

In **Figures 7– 9** the temperature dependence of magnetization in ZFC and FC modes is shown for GO-Fe₃O₄ nanoparticles and PTT-PTMO/GO-Fe₃O₄ nanocomposites. Four panels in each figure present $M(T)$ curves taken in four different magnetic fields: $H = 10, 100, 1000, \text{ and } 10000$ Oe. These figures display the characteristic thermal irreversibility anticipated for an assembly of single domain magnetic particles due to the blocking-unblocking process of magnetic moments during variation of

the thermal energy. In general, all samples display a rather broad size distribution of magnetic nanoparticles what is evidenced by the broadness of χ_{ZFC} curves and a large separation of the blocking temperature T_B (maximum in ZFC mode) and the irreversibility temperature T_{irr} (temperature of splitting of χ_{ZFC} and χ_{FC} curves). The latter is associated with the blocking of the biggest particles. Another evidence of a broad size distribution is no saturation of FC magnetization at low temperature. Comparison of **Figure 8** with **Figure 9** shows a very similar thermal behavior of magnetizations in both nanocomposites PTT-PTMO/0.3GO-Fe₃O₄ and PTT-PTMO/0.5GO-Fe₃O₄. On the other hand, comparison of magnetic susceptibilities of both nanocomposite samples with GO-Fe₃O₄ sample reveals a significant difference – nanocomposites seems to display two blocking temperatures, because two shallow maxima can be discerned in χ_{ZFC} curves, while only one maximum is visible in χ_{ZFC} curve of GO-Fe₃O₄ sample. Thus, the procedure of synthesis of polymer samples affects to some degree their magnetic properties producing bimodal-like distribution of the blocking temperatures. A simple explanation of this phenomenon involves the presence of a magnetite-polymer interface that produces the core-shell structure of magnetite nanoparticles in these samples. It is also apparent that there is no evidence of Verwey transition in magnetization curves in the neighborhood of 120 K. There is another interesting feature seen in the temperature dependence of magnetic susceptibility in both block copolymer samples that is absent in GO-Fe₃O₄. At low temperatures ($T < 20$ K) and in high magnetic fields ($H > 1$ kOe) it is manifested in the upturn in dc susceptibility of PTT-PTMO/0.3GO-Fe₃O₄ and PTT-PTMO/0.5GO-Fe₃O₄. Similar behavior was observed for composites of Fe₃O₄ nanoparticles with alginic acids [16]. It was interpreted in terms of the excitation of the spin waves with discrete spectrum. At higher temperatures, the magnetic energy levels are broadened and form a continuous excitation spectrum. In that case the temperature dependence of magnetization can be the same as in bulk materials. The proposed interpretation of magnetization upturn at low temperature assumes the presence of small nanoparticles because the involved quantum effects are magnified in restricted dimensions. Bimodal-like distribution of blocking temperatures in our polymer nanocomposite samples and the presence of magnetite-polymer interface suggest other

possible explanation of magnetization upturn at low temperature - ordering of spins in the nanoparticle shells in the magnetic field of already ordered spins in the magnetite cores [56].

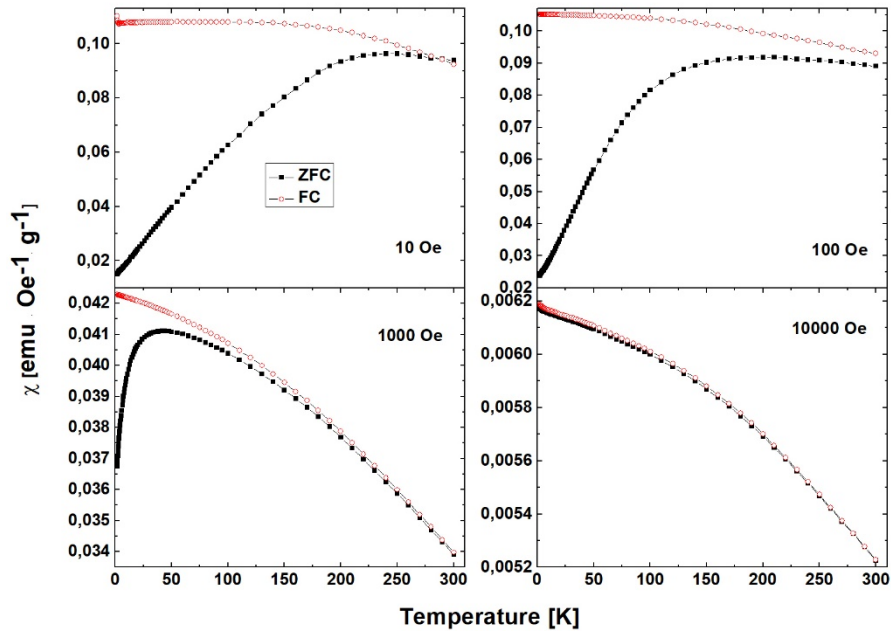


Figure 7. Temperature dependence of magnetic susceptibility in ZFC and FC modes in four magnetic fields (10, 100, 1000, and 10000 Oe) of GO-Fe₃O₄ sample.

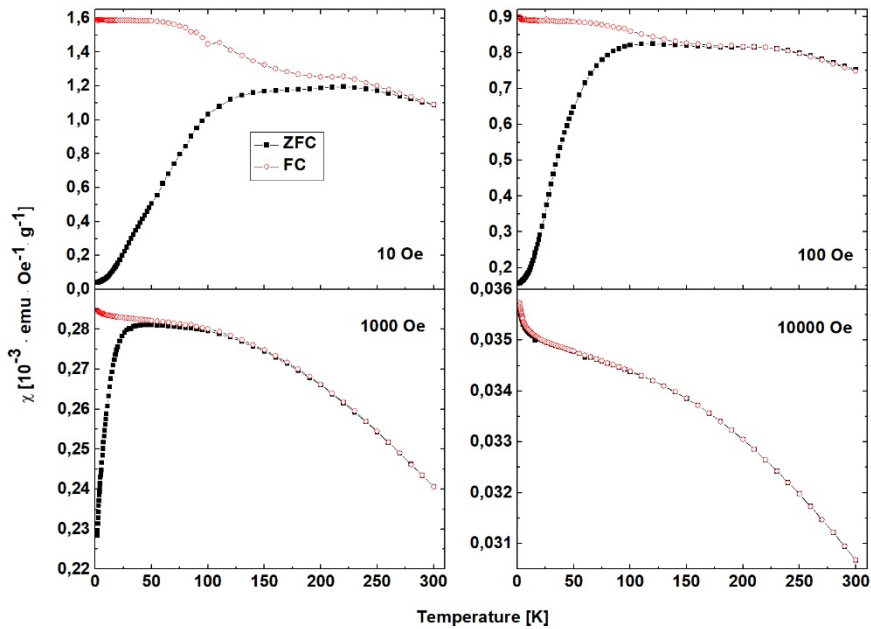


Figure 8. Temperature dependence of magnetic susceptibility in ZFC and FC modes in four magnetic fields (10, 100, 1000, and 10000 Oe) of PTT-PTMO/0.5GO-Fe₃O₄ sample.

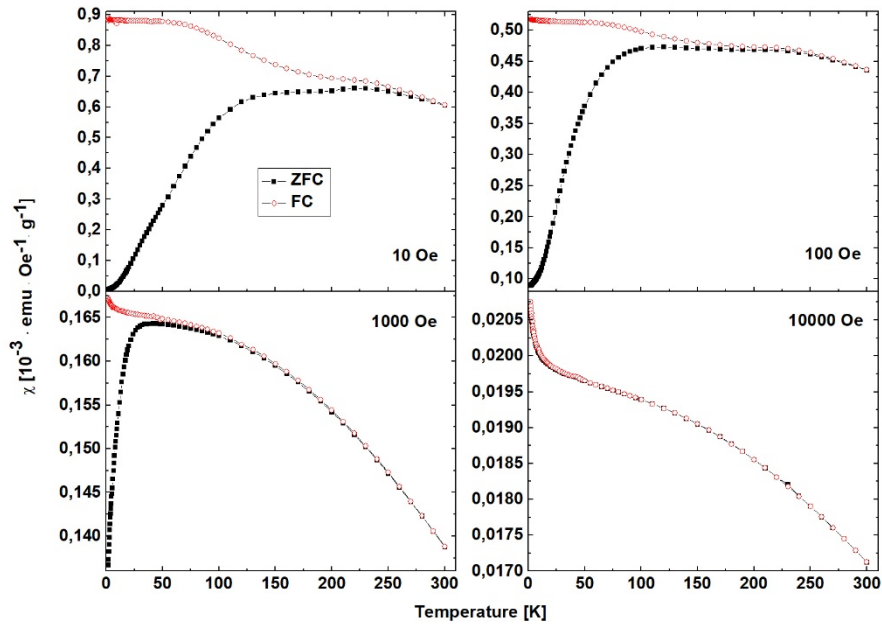


Figure 9. Temperature dependence of magnetic susceptibility in ZFC and FC modes in four magnetic fields (10, 100, 1000, and 10000 Oe) of PTT-PTMO/0.3GO-Fe₃O₄ sample.

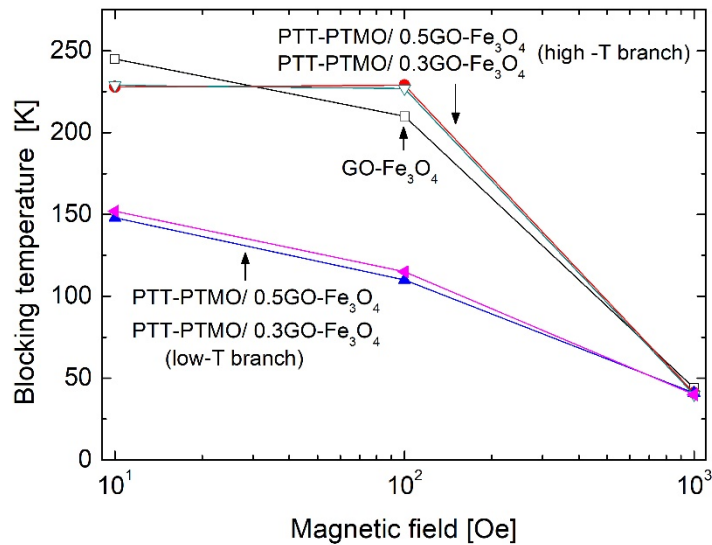


Figure 10. Dependence of the blocking temperature on external magnetic field in investigated GO-Fe₃O₄ and PTT-PTMO/GO-Fe₃O₄ nanocomposites. The solid lines are merely guides to the eyes.

The blocking temperature depends on applied magnetic field and is expected to shift to lower temperatures on increasing field strength because magnetic field lowers the barrier between two easy axis orientations. In **Figure 10** this dependence is presented for GO-Fe₃O₄ nanoparticles and

nanocomposites with their content. For both nanocomposites, as there are two blocking temperatures, there will be two branches of $T_B(H)$ curves. It is easy to see that the high temperature branch for GO- Fe_3O_4 and PTT-PTMO nanocomposites coincides and only the low temperature branch is specific for both nanocomposites samples. Double peaked M_{ZFC} could be explained to be the result of existence of two different subsystems of nanoparticles with different effective average sizes. The high temperature $T_B(H)$ branch represents one collection of larger nanoparticles in GO- Fe_3O_4 and PTT-PTMO nanocomposites and the low temperature branch is specific to PTT-PTMO nanocomposites. In the latter the core of a nanoparticle is effectively smaller because of the existence of a shell layer having different magnetic properties. Applying Eq. (3) to the common to all samples blocking temperature approximated to zero magnetic field ($T_B(0) = 250$ K) and using an average nanoparticle size obtained from TEM images ($D = 9$ nm), it can be calculated that $K = 2.2 \cdot 10^6$ erg cc^{-1} , what is much larger than that for bulk Fe_3O_4 ($1.35 \cdot 10^5$ erg cc^{-1} at RT). This enhancement of the particle's anisotropy is likely associated with a surface having larger anisotropy (aggregation of nanoparticles).

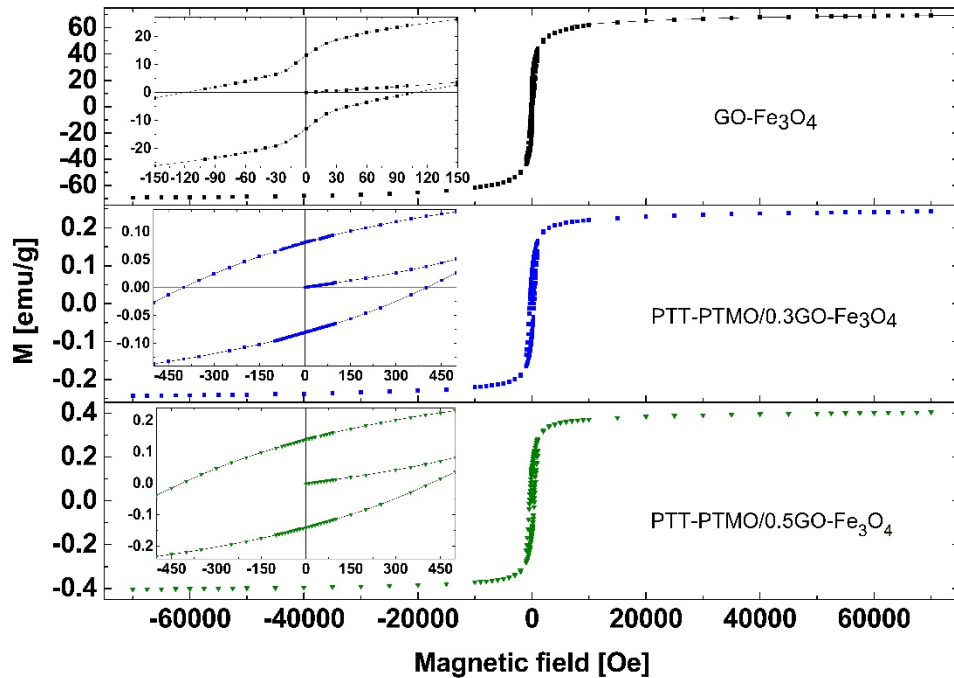


Figure 11. Isothermal magnetization at $T = 2$ K for GO- Fe_3O_4 and PTT-PTMO/ $\text{GO-Fe}_3\text{O}_4$ nanocomposites. The solid line in the upper panel is the fit to the sum of ferromagnetic and

paramagnetic components. The insets show expanded views of the low magnetic field behavior (the solid lines are guides for the eyes).

In **Figure 11** the isothermal (at $T = 2$ K) magnetizations of GO-Fe₃O₄ and PTT-PTMO/GO-Fe₃O₄ nanocomposites in magnetic fields up to 70 kOe are presented. As anticipated, magnetization in form of hysteresis loop is observed as the samples are in the blocked, ferromagnetic state. The diamagnetic contribution of polymer matrix has been subtracted in case of PTT-PTMO/0.3GO-Fe₃O₄ and PTT-PTMO/0.5GO-Fe₃O₄ samples. On the other hand, at RT no hysteresis loop is registered because this temperature is higher than the blocking temperature and the samples are in superparamagnetic state. The parameters of the observed loops (saturation magnetization, remanent magnetization, coercive field) at $T = 2$ K are listed in **Table 4**.

Table 4. Hysteresis loop parameters at $T = 2$ K of GO-Fe₃O₄ and PTT-PTMO/GO-Fe₃O₄ nanocomposites. Saturation and remanent magnetizations are expressed on a unit mass (1 g) of the whole sample, including GO and polymer masses.

Sample	H_c [Oe]	M_R [emu g ⁻¹]	M_s [emu g ⁻¹]	M_R/M_s
GO-Fe ₃ O ₄	114	13.2	69.3	0.19
PTT-PTMO/0.3GO-Fe ₃ O ₄	400	0.08	0.24	0.33
PTT-PTMO/0.5GO-Fe ₃ O ₄	415	0.14	0.40	0.35

The values of the saturation magnetization and the remanent magnetization in **Table 4** are calculated for a unit mass (1 g) of the whole sample, including GO and copolymer masses. Taking into account that in 1 g of GO-Fe₃O₄ sample the mass of magnetite is 0.686 g (this can be calculated from XPS data) it follows that the saturation magnetization would be 101 emu g⁻¹_(Fe₃O₄). This is slightly more than for bulk magnetite at that low temperature. But this value has to be reduced because the registered magnetization of GO-Fe₃O₄ sample do not reaches saturation even in 70 kOe magnetic field. Thus, the observed signal were treated as composed from two components: ferromagnetic, saturated below

20 kOe and paramagnetic that will not be saturated in the highest applied magnetic fields. By subtracting the paramagnetic signal from the observed data, the remaining ferromagnetic magnetization could be obtained. Magnetization of the paramagnetic component was approximated by Langevin function. The classical Langevin expression describes magnetization of uncoupled array of magnetic moments or an exchange coupled superparamagnetic array of magnetic moments (when the direction of the easy axis does not play a role)

$$M = M_S \left(\coth(x) - \frac{1}{x} \right), \quad (4)$$

where M_S is saturation magnetization, $x = \frac{\mu H}{kT}$ is the ratio of magnetic to thermal energy, μ is the magnetic moment and k is Boltzmann's constant. Fitting of $M(H)$ curve for GO-Fe₃O₄ sample in 20 – 70 kOe range by the sum of Eq. (4) and a constant (representing already saturated ferromagnetic component) was very accurate and gave the saturation magnetization of the ferromagnetic component to be 99 emu g⁻¹(Fe₃O₄) and the paramagnetic moment of 2.7 μ_B (Bohr magnetons). The fit is shown in **Figure 11** (upper panel) by a solid line.

Comparison of the values of the other loop parameters (H_c and M_R/M_S) for GO-Fe₃O₄ with both nanocomposite samples brings up a striking difference between them (**Table 4**). The coercive field is roughly three times and the M_R/M_S ratio (the squareness ratio coefficient Q) is two times bigger in the PTT-PTMO/GO-Fe₃O₄ nanocomposites in comparison with GO-Fe₃O₄. For non-interacting, randomly oriented particles with uniaxial magnetocrystalline anisotropy $Q = 0.5$, while for particles with cubic magnetocrystalline anisotropy $Q = 0.831$ [57]. As the squareness ratio represents the fraction of blocked particles at a specific temperature, its value increase with decrease of temperature [58]. Small values of this parameters indicate that the individual particles are single domains and display a strong random anisotropy [59]. Reduction of Q could be due to different reasons like inter-particle interaction, distribution of particle sizes, the presence of various defects, etc. Petrychuk et al. [60] investigated samples containing interacting magnetic nanoparticles forming clusters of different sizes. For small size magnetic clusters, the magnetic energy may be small enough to enable thermal energy the enhancement of the superparamagnetic contribution into magnetization. This results in

small values of coefficient Q . On the other hand, for larger cluster the magnetic energy is high what leads to the corresponding enhancement of its superferromagnetic properties. The hysteresis loop becomes more rectangular and the squareness ratio coefficient increases. These considerations suggest that Q value might be considered as a measure of cluster sizes in a strongly interacting system of ferromagnetic nanoparticles. Enhancement of the coercive field in both nanocomposite samples in comparison to GO-Fe₃O₄ might be explained by bigger contribution of the shape anisotropy in the former samples [57, 61, 62]. It has been shown that in the case of magnetic nanowires the coercivity can be evaluated from expression containing two terms - one related to the shape anisotropy and the other to the magnetocrystalline anisotropy. In case of specifically arranged nanoparticle assemblies the first term can be dominating. This might be the case of our nanocomposite samples were chains of Fe₃O₄ nanoparticles would ensure high value of the coercive field. **Figure 12** shows magnetization curves of each sample registered at RT. The data is plotted as M/M_S (dimensionless) vs. H to compare the shapes of the curves.

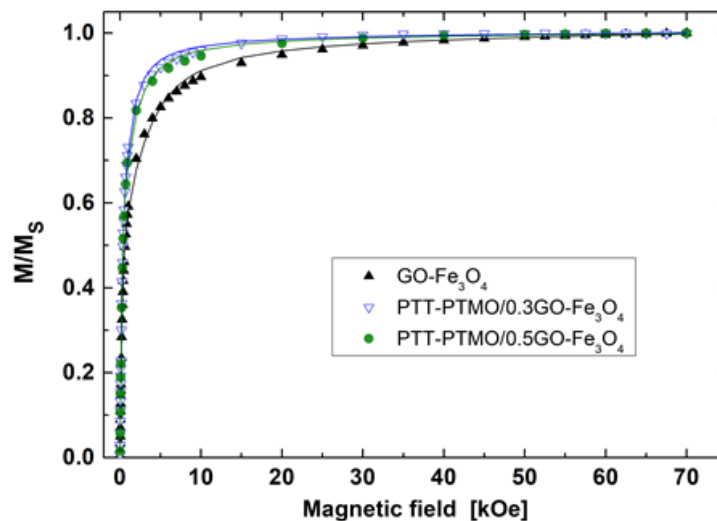


Figure 12. Normalized magnetization of GO-Fe₃O₄ and PTT-PTMO/GO-Fe₃O₄ nanocomposites in an external magnetic field at $T = 300$ K. The solid lines are the least-squares fits to the sum of two Langevin functions with different magnetic moments and a small term linear in magnetic field.

For PTT-PTMO/0.3GO-Fe₃O₄ and PTT-PTMO/0.5GO-Fe₃O₄ nanocomposites the curves are very similar, but GO-Fe₃O₄ nanoparticles hybrid showed a smaller magnetization in fields of intermediate

strengths and a slower approach to saturation. The magnetization curves in **Figure 12** cannot be adequately fitted using a single Langevin function with a single magnetic moment. Satisfactory fits of the data (solid lines in **Fig. 12**) were obtained using the sum of two Langevin functions corresponding to two different magnetic moments (differing by a factor of 10) and an additional small term linear in magnetic field. The obtained magnetic moments probably do not have much physical meaning, there are only indication of a spread of magnetic moment values (and corresponding nanoparticle sizes) in our samples [63]. Reduction of magnetization in intermediate fields in case of sample GO-Fe₃O₄ might be explained by an inter-particle interaction causing formation of flux closer loops [64].

Ferromagnetic resonance. Selection of FMR spectra in the form of magnetic field dependence of the field derivative of the microwave absorption registered at different temperatures in 90 - 300 K range is presented in **Figure 13** for GO-Fe₃O₄ (upper panel) and PTT-PTMO/0.5GO-Fe₃O₄ nanocomposite (lower panel).

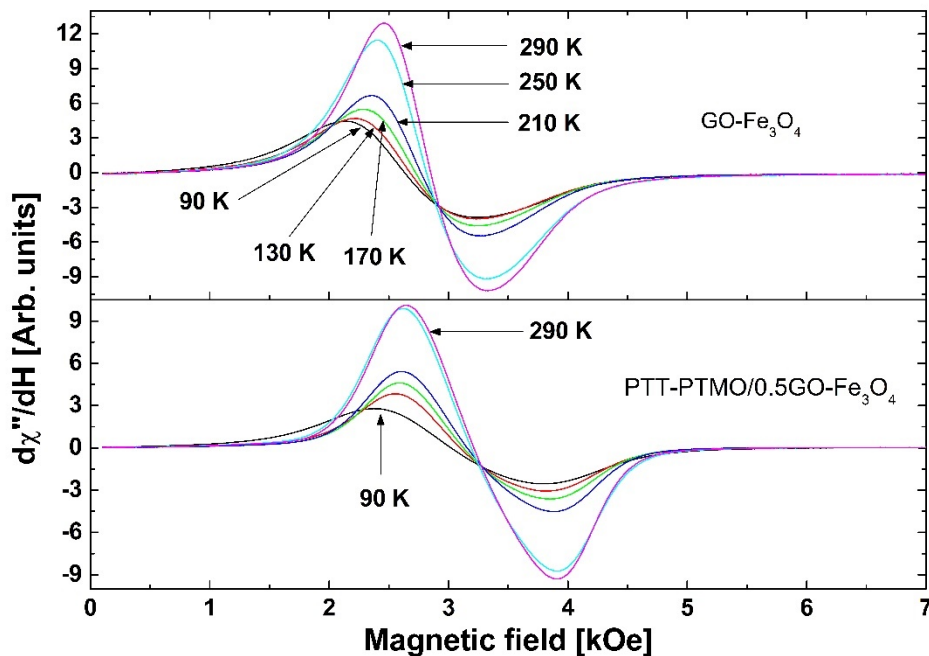


Figure 13. FMR spectra registered at different temperatures of GO-Fe₃O₄ (top panel) and PTT-PTMO/0.5GO-Fe₃O₄ nanocomposite (lower panel).

All FMR spectra are dominated by an intense, broad and asymmetrical line. The registered FMR spectra reflect very complex spatial arrangements of magnetic particles and a broad range of different interactions they are involved. To obtain information, albeit approximate and limited, about particles and their interactions, the spectra were decomposed on components described by Gaussian line shape functions [65, 66, 67]. Two Gaussian components were needed to obtain a very good agreement between the experimental and calculated spectra. As a result of fitting the values of the resonance field, linewidth and amplitude of each component were obtained at specific temperatures. Another important parameter – the integrated intensity – was calculated as the product of the amplitude and the square of linewidth. The results of fittings are presented in **Figures 14, 16, and 17** which show the temperature dependence of the resonance fields, linewidths, and integrated intensities, respectively.

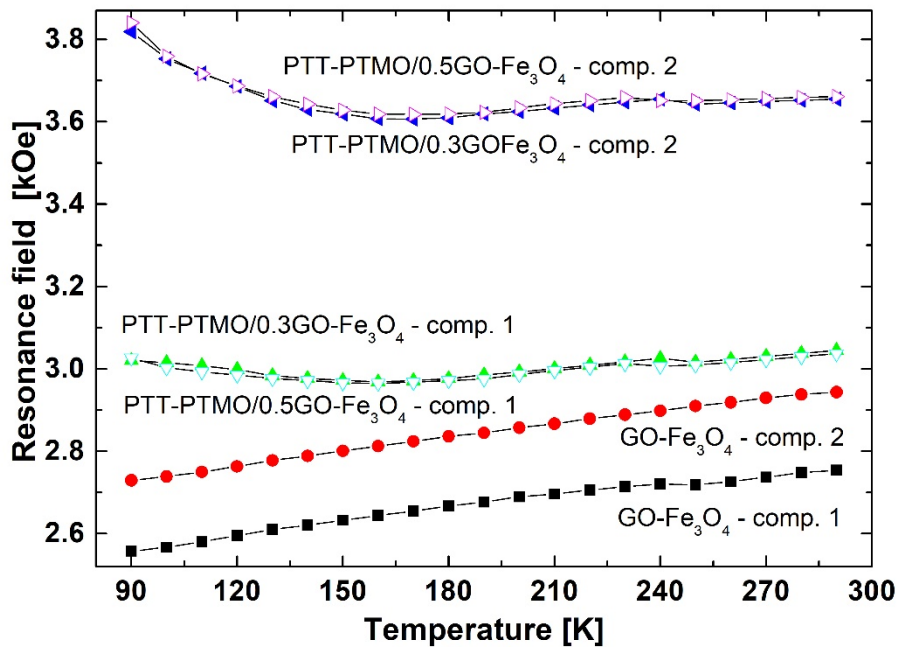


Figure 14. Temperature dependence of the resonance fields of the component lines (designated as comp. 1 and comp. 2) for GO-Fe₃O₄ and nanocomposites. The solid lines are guides for the eyes.

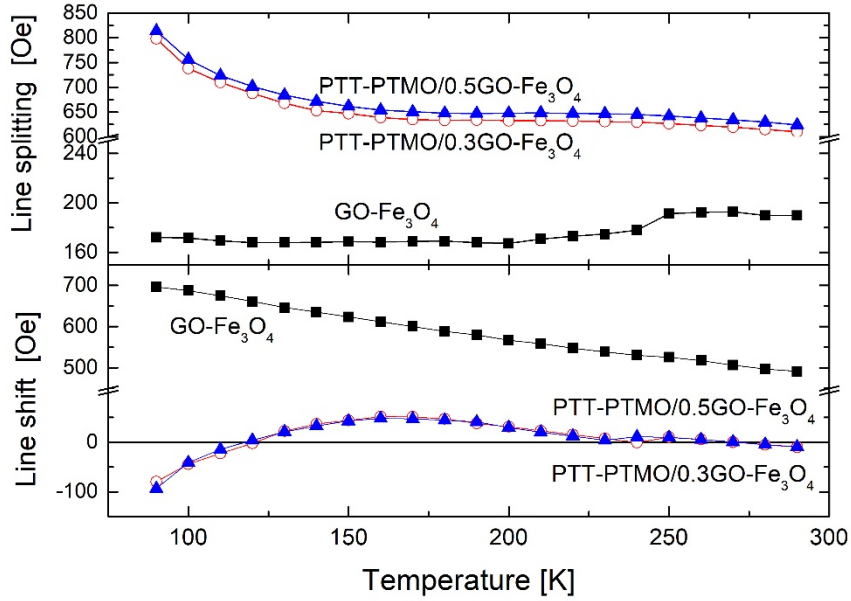


Figure 15. Temperature dependence of the line splitting between two components (top panel) and line shift (bottom panel) from magnetic field corresponding to $g = 2$ for GO-Fe₃O₄ and PTT-PTMO/GO-Fe₃O₄ nanocomposites.

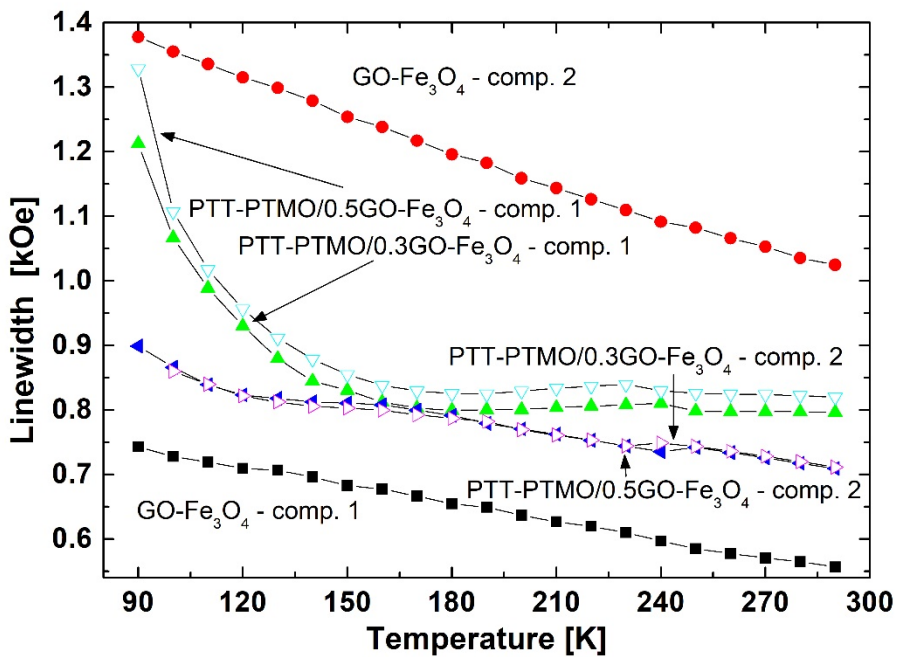


Figure 16. Temperature dependence of the linewidths of the component lines for GO-Fe₃O₄ and PTT-PTMO/GO-Fe₃O₄ nanocomposites. The solid lines are guides for the eyes.

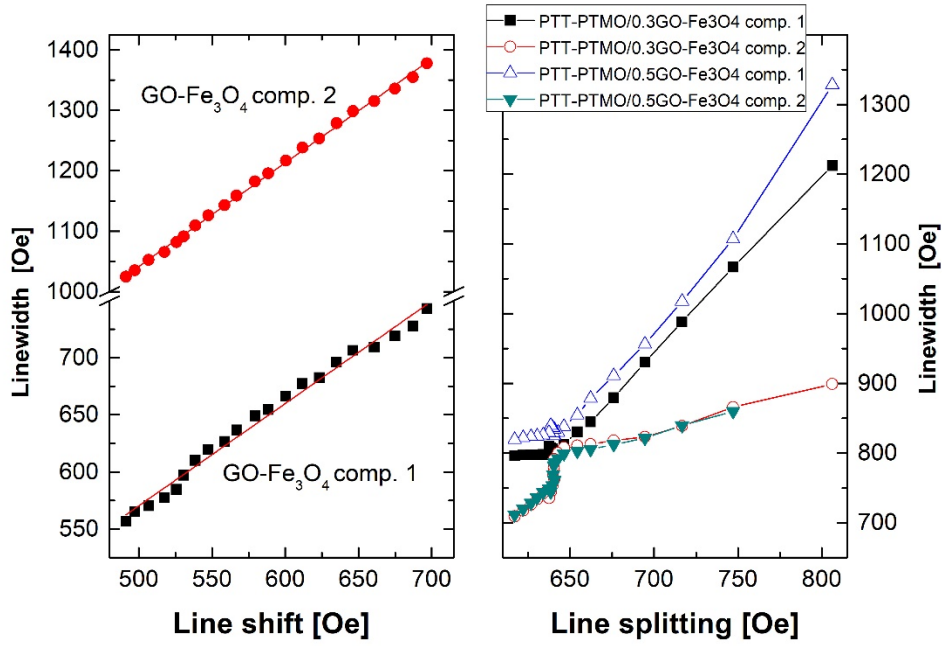


Figure 17. Dependence of component linewidth on the line shift from the reference field H_{r0} in GO-Fe₃O₄ (left panel) and on the line splitting in PTT-PTMO/GO-Fe₃O₄ nanocomposites (right panel). Solid lines in the left panel are linear fits, in the right panel are guides for the eyes.

A remarkable difference between the two studied polymer nanocomposite samples on the one hand, and the GO-Fe₃O₄ on the other hand, is seen in **Figure 14** that illustrates the temperature dependence of the resonance field of each component (designated as comp. 1 and comp. 2) for three studied samples. Two characteristic features of these dependencies are easily to notice: there is a different splitting of the two components in polymer as compared to GO-Fe₃O₄ samples (large for the former and small for the latter) and there is a different shift of the split components from the magnetic field H_{r0} corresponding to $g = 2$ (no internal field, superparamagnetic case) in both types of samples. These differences are illustrated in **Figure 15**. Top panel in **Fig.15** displays the temperature variation of the line split into two components in our three samples. Both polymer nanocomposites show a similar, large splitting of approximately 700 Oe, while that splitting in GO-Fe₃O₄ sample is significantly reduced and below 200 Oe. It is interesting to notice that similar differences were observed for the coercive fields in these samples what suggests a common mechanism behind those two different

phenomena. Bottom panel in Fig. 15 shows the temperature dependence of the line shift defined as the difference between H_{r0} (in our case $H_{r0} = 3340$ Oe) and the magnetic field in the middle between comp. 1 and comp. 2 lines. Contrary to the case of line splitting this shift is large for GO-Fe₃O₄ (above 500 Oe and increasing with temperature decrease) and small (below 100 Oe) for both polymer nanocomposites. The reasons for these differences should be searched in morphological differences between GO-Fe₃O₄ and both PTT-PTMO/GO-Fe₃O₄ nanocomposites. In the following the large shift of the resonance line from H_{r0} in GO-Fe₃O₄ will be explained by agglomeration of magnetite nanoparticles in that sample and the large split of two components in both polymer nanocomposites by a significant contribution of the surface energy due to a strong polymer and magnetite interface.

Study of temperature dependence of the resonance field in FMR experiments could provide valuable information on spin dynamics of ferromagnetic nanoparticles [68, 69, 70]. In FMR studies the following resonance condition must be satisfied: $\omega_0 = \gamma \cdot H_{eff}$, where ω_0 is the microwave frequency, γ the gyromagnetic ratio for electron, H_{eff} the effective magnetic field which is the vector sum of externally applied field and an intrinsic field. The latter field could have a few components, like magnetocrystalline anisotropy field H_a , shape anisotropy field H_s , dipolar field H_D , exchange field H_{ex} , etc. The number of field components depends on physical and chemical characteristics of particular nanomaterial. Considering FMR line splitting observed in our samples, an expression containing three terms is necessary: the Zeeman term, and two terms describing different anisotropies: surface anisotropy and bulk (volume) magnetocrystalline anisotropy. The volume term, proportional to K_V (volume anisotropy constant) is standard and may be regarded as a uniform intrinsic field H_a independent on particle size. There is a simple relation between these quantities

$$H_a = \frac{2K_V}{M} \quad (5)$$

where M is magnetization. The surface anisotropy term contains K_s (surface anisotropy constant) and acts like an additional uniform field. Its strength depends on particle size the smaller the particle the

stronger that field. The equations for both resonance fields of the two split components are the following [71]:

$$H_r(1) = \frac{\omega_0}{\gamma} - \frac{6K_s}{RM} - H_a \quad (6)$$

when the external field is parallel to the anisotropy axis, and

$$H_r(2) = \frac{\omega_0}{\gamma} + \frac{3K_s}{RM} + \frac{H_a}{2} \quad (7)$$

when the field is perpendicular to the axis. In Eq. (6) and (7) R stand for the radius of a nanoparticle.

Subtracting Eqs. (6) and (7) and multiplying the result by $2/3$, one gets

$$\frac{2}{3}[H_r(2) - H_r(1)] = \frac{6K_s}{RM} + H_a \quad (8)$$

In our samples the spread of anisotropy axes is random so in fact only a single broad line is registered, but its decomposition on two components allow to find resonance fields in Eqs. (6) and (7). For GO-Fe₃O₄ sample the surface term (the first in the right-hand side in Eq. (8)) could be omitted as the bulk magnetocrystalline energy is supposed to be bigger than the surface energy. In that case the anisotropy field H_a calculated from the line splitting (~ 180 Oe) in GO-Fe₃O₄ is equal to 120 Oe. This value is very close to the coercive field in this sample measured in isothermal magnetization. Actually, this is to be expected as for the coercive field H_c the same equation as for H_a is valid (see Eq. (5)). If the anisotropy field is the same in both polymer nanocomposites as in GO-Fe₃O₄, than Eq. (8) allows to calculate the surface anisotropy constant K_s . Substituting ~ 700 Oe for the line splitting, $R = 4.5$ nm, and $M = 90$ emu g⁻¹, the value of 0.15 erg cm⁻² for K_s is obtained. The surface of magnetite nanoparticles can be strongly influenced by bonding to the polymer matrix.

A large shift of FMR lines from the reference field H_{r0} in GO-Fe₃O₄ sample could be explained by agglomeration of magnetite nanoparticles in form of elongated assemblies along the lines of an external magnetic field. In contrast, in PTT-PTMO nanocomposites the polymer matrix prevents such rearrangements so the FMR shift is expected to be small or vanishing. Shape anisotropy field H_s

depends on the relative value of the three orthogonal demagnetization factors, N_a , N_b , and N_c , where $N_a + N_b + N_c = 4\pi$. For elongated particles or assemblies ($N_a = N_b$), $H_S = (N_a - N_c) \cdot M_S = \Delta N \cdot M_S$, where M_S is the saturation magnetization. For elongated needles ($N_a = N_b = 2\pi$, $N_c = 0$), $H_S = 2\pi M_S$. The shape anisotropy field is adding as a vector to the external magnetic field. If elongated aggregate of nanoparticles is situated parallel to the external field directions, the following well known equations could be use:

$$\frac{\omega_0}{\gamma} = H_r + \Delta N \cdot M_S \quad (9)$$

According to this equation the observed resonance field H_r decreases by a factor proportional to the saturation magnetization and the difference of the demagnetization factors. The observed increase of the shift for GO-Fe₃O₄ sample with decreasing temperature can be explained by increase of magnetization. The value of ΔN calculated from Eq. (9) is approximately 0.10 for GO-Fe₃O₄. Although this particular approach to orientation dependence of the resonance field in FMR experiment seems adequate for our sample, more general one was previously reported [72, 73, 74].

In **Figure 16** the temperature dependence of the linewidths of the component lines for the three investigated samples is displayed. In general, all linewidths increase with decreasing temperature. This is usually attributed to a gradual suppression of the averaging effect of thermal fluctuations with decreasing temperature [75, 76]. The linewidths of two components in GO-Fe₃O₄ show almost linear increase during cooling down this sample from RT and the largest linewidth is found for the perpendicular component (comp. 2 in **Figure 16**). Line components linewidths in both nanocomposites display more complex thermal behavior, but a general tendency of increasing with temperature decrease is easily recognized, especially below 150 K. The observed temperature dependence of components linewidths shows a remarkable similarity to the temperature dependence of internal fields producing shift and splitting of FMR lines (see **Figure 15**). This is illustrated in **Figure 17** where the dependence of the component linewidths as a function of the line shift from the reference field H_{r0} in GO-Fe₃O₄ and on the line splitting in the PTT-PTMO/GO-Fe₃O₄ nanocomposites is presented.

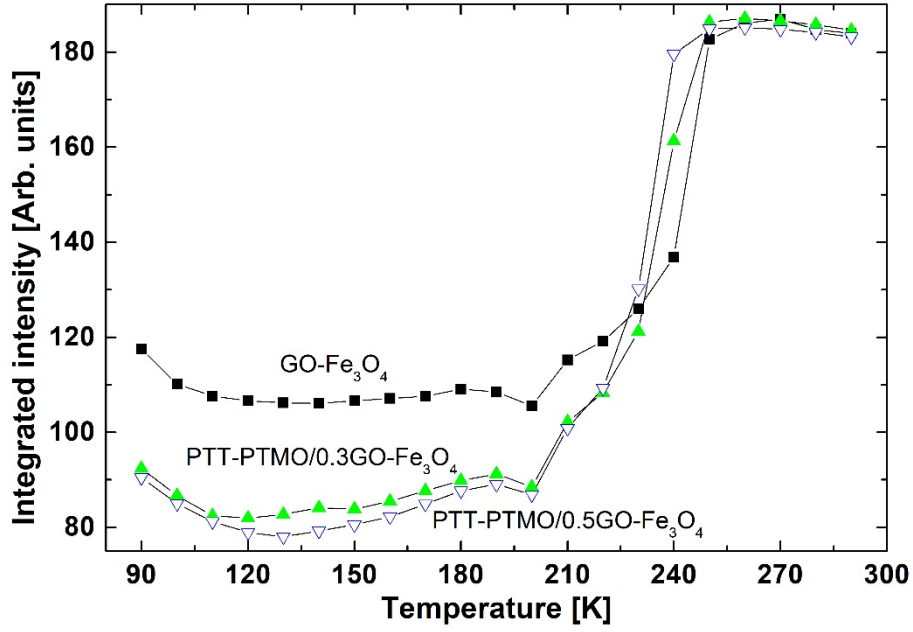


Figure 18. Temperature dependence of the normalized (at RT) integrated intensities for the GO-Fe₃O₄ and PTT-PTMO/GO-Fe₃O₄ nanocomposites. The solid lines are guides for the eyes.

The observed trend in linewidth broadening clearly indicate inhomogeneous broadening created by the spread of easy-axis directions in regard to appropriate internal field (demagnetization field in case of GO-Fe₃O₄ and surface anisotropy field in case of polymer nanocomposite samples) as a major contributor to the linewidth [20]. On the other hand, it could not be the only factor that determines the component linewidth because the observed linewidths are bigger than the appropriate internal fields. Other factors, like distribution of nanoparticle or cluster sizes should also have an effect on the observed component linewidth because size distribution influences directly the magnitude of the internal fields [75, 76].

In **Figure 18** the temperature dependence of the normalized (at RT) integrated FMR intensities I_{FMR} (calculated as the sum of two components) for the PTT-PTMO/GO-Fe₃O₄ nanocomposites and GO-Fe₃O₄ is presented. $I_{FMR}(T)$ curves show a very interesting behavior. Initial cooling from RT causes a slight increase of I_{FMR} , but near 260 K a very rapid drop of FMR intensity is observed for GO-Fe₃O₄ and PTT-PTMO based nanocomposites. The magnitude of this decrease is slightly smaller for GO-Fe₃O₄ (40 % drop) than for both polymer nanocomposites (60 % drop). This might be explained by

relatively more intense FMR spectrum of the latter samples at high temperatures in comparison to GO-Fe₃O₄ sample. Because the behavior of $I_{FMR}(T)$ is similar to $\chi_{ZFC}(T)$ it is possible to introduce the notion of FMR blocking temperature. It is surprisingly close to the blocking temperature determined from dc magnetization. FMR measurements should give a much higher value of the blocking temperature than determined from SQUID magnetization since the time windows τ for the two methods are very different: $\tau_{FMR} \sim 10^{-9}$ s, $\tau_{SQUID} \sim 10^2$ s [77]. But as was noticed by Ramos et al. [78] the notion of blocking in FMR has different meaning than in SQUID magnetization. That difference is the consequence of the fact, that in FMR the measurements are done in much stronger magnetic fields (~a few kOe) than in magnetization studies (only a few Oe). In consequence, if the effective anisotropy field becomes greater than H_{r0} the nanoparticles whose easy axes are close to the direction of the applied field will no longer reach the resonance condition and a drop in FMR intensity will be registered. This idea might be supported by the observation that the components with the largest linewidth have the biggest contribution to the FMR intensity decrease below 260 K. Thus, the intensity decrease cannot be used as a feature that indicates the change from superparamagnetic to blocked regimes [79]. Because the magnitude of the internal anisotropy fields is similar in GO-Fe₃O₄ and PTT-PTMO/GO-Fe₃O₄ nanocomposites, FMR intensity drop is registered at a similar temperature ~260 K. On further cooling the I_{FMR} curve levels down and below 120 K starts to slowly increase on temperature decrease. This increase is probably correlated with magnetization increase on temperature decrease observed in SQUID magnetization studies.

Conclusions

The polyester thermoplastic elastomeric nanocomposites with improved phase separated structure were obtained by *in situ* polymerization. Homogenous dispersion of GO-Fe₃O₄ nanoparticle hybrid in the PTT-PTMO matrix was confirmed by the TEM analysis. The average size of Fe₃O₄ nanocrystals distributed on GO sheets was ca. 9 nm. Due to presence of GO-Fe₃O₄ in copolymer matrix and better phase separation the improvement of tensile properties of PTT-PTMO/GO-Fe₃O₄ nanocomposites was observed. Superparamagnetic behavior for GO-Fe₃O₄ hybrid nanoparticles and

nanocomposites with their content was observed at room temperature as well as hysteresis due to blocking of the magnetic dynamics at low temperature. A high value of 69.3 emu g⁻¹ for saturation magnetization in GO-Fe₃O₄ hybrid nanoparticles and 0.24 and 0.40 emu g⁻¹ for nanocomposites at loading of 0.3 and 0.5 wt% of GO-Fe₃O₄ in polyester thermoplastic elastomeric matrix, respectively, was registered.

Due to low toxicity and of GO-Fe₃O₄ hybrid nanoparticles [80, 81], the prepared elastomeric nanocomposites with their low loading could be developed for its potential application as a contrast agent in MRI, but this application requires further laboratory and in vivo investigations, especially with regard to the use of more biocompatible elastomer matrix. The used here PTT-PTMO thermoplastic elastomer as nanocomposite polymer matrix is more of an engineering material but it is possible to replace it by a more biocompatible elastomer, e.g. PTT-PEO copolymer [82] or PLA copolymer [81]. In surgical implants loaded with superparamagnetic GO-Fe₃O₃ hybrids acting as image contrast the sensitivity of MRI will be enhanced.

Appendix A. Supplementary material

Acknowledgments

Authors would like to thank DuPont Tate & Lyle Bio Products company for providing bio -1,3 propanediol for experimental use. Dris Ihiwakrim from IPCMS is acknowledged for performing TEM microscopy. Dr Matej Micusik from Polymer Institute of Slovak Academy of Sciences is acknowledged for XPS analysis. Zdenko Spitalsky gratefully acknowledge to VEGA 2/0093/16 for financial support.

Conflict of Interest

The authors declare no conflict of interest.

References

[1] M. Colombo, S. Carregal-Romero, M. F. Casula, L. Gutierrez, M.P. Morales, I. P. Bohm, J. T. Heverhagen, D. Prospero, W. J. Parak, Chem. Soc. Rev. 2012, 41, 4306.

- [2] P. Tartaj, M. P. Morales, T. Gonzalez-Carreno, S. Veintemillas-Verdaguer, C. J. Serna, *Adv. Mater.* **2011**, *23*, 5243.
- [3] L. H. Reddy, J. L. Arias, J. Nicolas, P. Couvreur, *Chem. Rev.* **2012**, *112*, 5818.
- [4] L. M. Rossi, N. J. S. Costa, F. P. Silva, R. Wojcieszak, *Green Chem.* **2014**, *16*, 2906.
- [5] S. R. Chowdhury, E. K. Yanful, A. R. Pratt, *J. Hazard. Mater.* **2012**, *235–236*, 246.
- [6] A. M. Bruck, C. A. Cama, C. N. Gannett, A.C. Marschilok, E.S. Takeuchi, K. J. Takeuchi, *Inorg. Chem. Front.* **2016**, *3*, 26.
- [7] L. Peng, J. Chao, M. Wen-Bo, B. Hai-Li, *Chin. Phys. B* **2013**, *22*, 047505.
- [8] Y. Liu, N. Tang, X. Wan, Q. Feng, M. Li, Q. Xu, F. Li, Y. Du, *Sci. Rep.* **2013**, *3*, 2566.
- [9] M. Wang, W. Huang, M. B. Chan-Park, Ch. M. Li, Magnetism in oxidized graphenes with hydroxyl groups, *Nanotechnology* **2011**, *22*, 105702.
- [10] R. M. Cornell, U. Schwertmann, *The Iron Oxides: Structures, Properties, Reactions, Occurrences and Uses, Second Edition*, Wiley-VCH, Weinheim, Germany, 2003.
- [11] T. Bodziony, N. Guskos, J. Typek, Z. Roslaniec, U. Narkiewicz, U., M. Kwiatkowska, M. Maryniak, *Rev. Adv. Mater. Sci.* **2004**, *8*, 86.
- [12] N. Guskos, S. Glenis, G. Zolnierkiewicz, J. Typek, P. Berczynski, A. Guskos, D. Silbera, U. Narkiewicz, *Appl. Phys. Lett.* **2012**, *100*, 122403.
- [13] T. Bodziony, N. Guskos, J. Typek, Z. Roslaniec, U. Narkiewicz, M. Kwiatkowska, M. Maryniak, *Mater. Sci. - Poland* **2005**, *23*, 1055.
- [14] B. Andrzejewski, W. Bednarski, M. Kazmierczak, K. Pogorzelec-Glaser, B. Hilczer, S. Jurga, M. Matczak, B. Leska, R. Pankiewicz, L. Kepinski, *Composite: Part B* **2014**, *64*, 147.

- [15] M. M. Noginov, N. Noginova, O. Amponsah, R. Bah, R. Rakhimov, V.A. Atsarkin, *J. Magn. Mater.* **2008**, 320, 2228.
- [16] O. N. Sorokina, A. V. Bychkova, A. L. Kovarskii, *Russ. J. Phys. Chem. B* **2009**, 3, 257.
- [17] J. B. Mamani, A.J. Costa-Filho, D. R. Cornejo, E. D. Vieira, L. F. Gamarra, *Mater. Character.* **2013**, 81, 28.
- [18] F. J. Owens, , *J. Phys. Chem. Solid.* **2003**, 64, 2289.
- [19] H. Li, M. T. Klem, K. B. Sebyy, D. J. Singel, M. Young, T. Douglas, Y. U. Idzerda, *J. Magn. Mater. Mater.* **2009**, 321, 175.
- [20] J. Kim, W. Ni, Ch. Lee, E. C Kan, E. C., Hosein, I. D., Song, Y., Liddell, Ch., *J. Appl. Phys.* **2006**, 99, 08R903.
- [21] M. Charilaou, K. K. Sahu, D. Faivre, A. Fisher, A., I. Garcia-Rubio, A. U. Gehring, *Appl. Phys. Lett.* **2011**, 99, 182504.
- [22] A. L. Kovarski, A. V. Bychkova, O. N. Sorokina, V. V. Kasparov, *Magnetic Resonance in Solids* **2008**, 10, 25.
- [23] B .P. Weiss, S. S. Kim, J. L. Kirschvink, R .E. Kopp, M. Sankaran, A. Kobayashi, A. Komeili, *Earth Planet. Sci. Lett.* **2004**, 224, 73.
- [24] J. L. Kirschvink, *Bioelectromag.* **1996**, 17, 187.
- [25] H. Sakuma, S. Sato, R. Gomimoto, S. Hiyama, K. Ishii, *IEEJ Trans.* **2007**, 2, 431.
- [26] J. C. Apesteguy, S. E. Jacobo, L. Lezama, G.V. Kurlyandskaya, N. N. Schegoleva, *Molecules* **2014**, 19, 8387.
- [27] V. N. Nikiforov, Yu. A. Koksharov, S. N. Polyakov, A. P. Malakho, A. V. Volkov, M. A. Moskvina, G. B. Khomutov, V. Yu. Irkhin, *J. All. Compd.* **2013**, 569, 58.

- [28] J. Landers, F. Stromberg, M. Darbandi, C. Schoppner, W. Keune, H. Wende, *J. Phys.: Condens. Matter* **2015**, *27*, 026002.
- [29] J. Wang, Q. Chen, X. Li, L. Shi, Z. Peng, Ch. Zeng, *Chem. Phys. Lett.* **2004**, *390*, 55.
- [30] M. A. Augustyniak-Jablokow, K. Tadyszak, M. Maćkowiak, Y. V. Yablokov, *Phys. Status Solidi RRL* **2011**, *5*, 271.
- [31] K. Tadyszak M. Mackowiak, M.A. Augustyniak-Janblokow, R. Strzelczyk, *J. Mol. Struct.* **2014**, *1076*, 31.
- [32] W. Wu, W., Z. Wu, Z., T. Yu, Ch. Jiang, W. S. Kim, *Sci. Technol. Adv. Mater.* **2015**, *16*, 023501.
- [33] B. Jaleh, A. Khalilipour, S. Habibi, M. Niyafar, M. Nasrollahzadeh, *J. Mater. Sci.: Mater. Electron.* **2017**, *28*, 4974.
- [34] O. Metin, S. Aydogan, K. Meral, *J. Alloys. Compd.* **2014**, *585*, 681-88.
- [35] J. Su, M. Cao, L. Ren, Ch. Hu, *J. Phys. Chem C* **2011**, *115*, 14469.
- [36] Y. Chandra, J. Park, Y. Chun, J.W. Lee, I.Ch. Hwang, K.S. Kim, *ACS Nano* **2010**, *4*, 3979.
- [37] H. Teymourian, A. Salimi, S. Khezrian, *Biosensors and Bioelectronics* **2013**, *49*, 1-8.
- [38] M. Nasrollahzadeh, M. Atarod, S. M. Sajadi, *J. Colloid Interf. Sci.* **2017**, *486*, 153.
- [39] M. Atarod, M. Nasrollahzadeh, S. M. Sajadi, *RSC Adv.* **2015**, *5*, 91532.
- [40] M. Nasrollahzadeh, M. Maham, A. Rostami-Vartooni, M. Bagherzadeh, S. M. Sajadi, *RSC Adv.* **2015**, *5*, 64769.
- [41] M. Maham, M. Nasrollahzadeh, S.M. Sajadi, M. Nekoei, *J. Colloid Interf. Sci.* **2017**, *497*, 33.
- [42] A. Omidvar, B. Jaleh, M. Nasrollahzadeh, H. R. Dasmeh, *Chem. Eng. Res. Des.* **2017**, *121*, 339.

- [43] M. Atarod, M. Nasrollahzadeh, S. M. Sajadi, *J. Colloid Interf. Sci.* **2016**, *465*, 249.
- [44] B. Shen, W. Zhai, M. Tao, J. Ling, W. Zheng, Lightweight, multifunctional polyetherimide/grapheneFe₃O₄ composite foams for shielding electromagnetic pollution, *ACS Appl. Mater. Interfaces* **2013**, *5*, 11383.
- [45] S. Paszkiewicz, A. Szymczyk, Z. Špitalský, J. Mosnáček, K. Kwiatkowski, Z. Roslaniec, *Eur. Polym. J.*, **2014**, *50*, 69.
- [46] S. Paszkiewicz, A. Szymczyk, K. Livanov, H.D. Wagner, Z. Roslaniec, *eXPRESS Polym. Lett.* **2015**, *9*, 509.
- [47] S. Paszkiewicz, A. Szymczyk, X. M. Sui, H. D. Wagner, A. Linares, T.A. Ezquerra, Z. Roslaniec, *Compos. Sci. Technol.* **2015**, *118*, 72.
- [48] S. Paszkiewicz, A. Szymczyk, R. Pilawka, B. Przybyszewski, A. Czulak, Z. Roslaniec, *Adv. Polym. Technol.* **2017**, *36*, 236.
- [49] Z. Spitalsky, M. Danko, J. Mosnacek, *Curr. Orag. Chem.* **2011**, *15*, 1133.
- [50] S. Laurent, D. Forge, M. Port, A. Roch, C. Robic, L.V. Elst, R. N. Muller, *Chem. Rev.* **2008**, *108*, 2064.
- [51] G. A. Dorofeev, A. N. Streletskii, I. V. Povstugar, A. V. Protasov, E. P. Elsukov, *Colloid J.* **2012**, *74*, 710.
- [52] A. Szymczyk, J. Nastalczyk, R. J. Sablong, Z. Roslaniec, *Polym. Adv. Technol.* **2011**, *22*, 72.
- [53] D. M. Marcano, D. V. Kosynkin, J. B. Berlin, A. Sinitsjii, Z. Sun, A. Slesarev, L. B. Alemany, W. Li, J. M. Tour, *ACS Nano* **2010**, *4*, 4806.
- [54] A. Szymczyk, S. Paszkiewicz, I. Pawelec, S. Lisiecki, Z. Špitalský, J. Mosnáček, Z. Roslaniec, *J. Nanomat.* **2015**, Article ID 382610.

- [55] M. Knobel, W. C. Nunes, L. M. Socolovsky, E. De Biasi, J. M. Vargas, and J. C. Denardin, *J. Nanosci. Nanotechnol.* **2008**, *8*, 2836.
- [56] J. Mantilla, L. León Félix, M. A. R. Martinez, P. Souza, P. A. M. Rodrigues, L. C. Figueiredo, S. W. da Silva, J. A. H. Coaquira, F. F. H. Aragón, P. C. Morais, *J. Magn. Magn. Mater.* **2019**, *476*, 392.
- [57] J. Garcia-Otero, M. Porto, J. Rivas, A. Bunde, *J. Appl. Phys.* **1999**, *85*, 2287.
- [58] V. Spasojevic, A. Mrakovic, M. Perovic, V. Kusigerski, J. Blanusa, *J. Nanopart. Res.* **2011**, *13*, 763.
- [59] N. E. Fenineche, R. Hamzaoui, O. El Kedim, *Mater. Lett.* **2003**, *57*, 4165.
- [60] M. Petrychuk, V. Kovalenko, A. Pud, N. Ogurtsov, A. Gubin, *Phys. Status Solidi A Appl. Mater.* **2010**, *207*, 442.
- [61] B. Duong, H. Khurshid, P. Gangopadhyay, J. Devkota, K. Stojak, H. Srikanth, L. Tetard, R.A. Norwood, N. Peyghambarian, M.H. Phan, J. Thomas, *Small* **2014**, *10*, 2840.
- [62] L. Sun, Y. Hao, C. L. Chien, P. C. Searson, *IBM J. Res. Dev.* **2005**, *49*, 79.
- [63] N. L. Adolphi, D. L. Huber, H. C. Bryant, T. C. Monson, D. L. Fegan, J. Lim, J. E. Trujillo, T. E. Tessier, D. M. Lovato, K. S. Butler, P. P. Provencio, H. J. Hathaway, S. A. Majetich, R. S. Larson, E. R. Flynn, *Phys. Med. Biol.* **2010**, *55*, 5985-6003.
- [64] R. W. Chantrell, M. Walmsley, J. Gore, M. Maylin, *Phys. Rev. B* **2000**, *63*, 024410.
- [65] P. C. Morais, G. R. R. Goncalves, K. Skeff Neto, F. Pelegrini, N. Buske, *IEEE Trans. Magn.* **2002**, *38*, 3225.
- [66] G. R. R. Goncalves, A. F. Bakuzis, K. Skeff Neto, F. Pelegrini, P. C. Morais, *J. Magn. Magn. Mater.* **2005**, *289*, 142.

- [67] L. L. Castro, G. R. R. Goncalves, K. Skeff Neto, P. C. Morais, A. F. Bakuzis, R. Miotto, *Phys. Rev. E* **2008**, 78, 061507.
- [68] E. Wajnberg, D. Acosta-Avalos, L. J. El-Jaick, L. Abracado, J. L. A. Coelho, A. F. Bakuzis, P. C. Morais, D. M. S. Esquivel, *Biophys. J.* **2000**, 78, 1018.
- [69] G. R. R. Goncalves, A. R. Pereira, A. F. Bakuzis, K. Skeff Neto, F. Pelegrini, P. C. Morais, *J. Magn. Magn. Mater.* **2001**, 226-230, 1896.
- [70] P.C. Morais., J.G. Santos, K. Skeff Neto, F. Pelegrini, M. De Cuyper, *J. Magn. Magn. Mater.* **2005**, 293, 526.
- [71] V. P. Shilov, J.-C. Bacri, F. Gazeau, F. Gendron, R. Perzynski, L. Yu, L. Raikher, *J. Appl. Phys.* **1999**, 85, 6642.
- [72] J. F. Saenger, K. Skeff Neto, P. C. Morais, M. H. Sousa, F. A. Tourinho, *J. Magn. Magn. Mater.* **1998**, 143, 180.
- [73] L. C. Figueiredoa, B. M. Lacavaa, K. Skeff Netoa, F. Pelegrinib, P. C. Moraisa, *J. Magn. Magn. Mater.* **2008**, 320, e347.
- [74] A. F. Bakuzis, P. C., Morais, F. Pelegrini, *J. Appl. Phys.* **1999**, 85,7480.
- [75] P. C. Morais, M. C. L. Lara, K. Skeff Neto, *Phil. Mag. Lett.* **1987**, 55, 181.
- [76] P. C. Morais, M. C. H. L. Lara, F. A. Tourinho *J. Magn. Magn. Res. Series A* **1996**, 121, 70.
- [77] D. S. Schmool, H. Kachkachi, Collective effects in assemblies of magnetic nanoparticles, *Solid State Phys.* **2016**, 67, 1-101.
- [78] C. A. Ramos, E. V. Brigneti, E. De Biasi, M. Vázquez, in *Nanowires - Fundamental Research*, (Ed: A. A. Hashim), InTech Open, London, UK, 2011, Ch. 15, pp. 333-356.

- [79] E. De Biasi, E. Lima Jr., C. A. Ramos, A., Butera, R. D. Zysler, *J. Magn. Magn. Mater.* **2013**, 326, 138-146.
- [80] M. Rahman, S. Beg, M. Z. Ahmad, F. Anwar, V. Kumar, in. *Graphene Science Handbook: Size Dependent Properties* (Eds: M. Aliofkhazraei, N. Ali, W. I. Milne, C. S. Ozkan, S. Mitura, J. L. Gervasoni), CRS Press Taylor & Francis Group, Boca Raton, FL, 2016, Ch. 26, p. 408.
- [81] J. Paulo Davim, *Biomedical Composites: Materials, Manufacturing and Engineering*, Walter de Gruyter GmbH & Co. KG., Berlin/Boston, Germany, 2014.
- [82] E. Piesowicz, A. Szymczyk, S. Paszkiewicz, *Polymers* **2016**, 8, 237.